Available online at www.sciencedirect.com
ScienceDirect
Trans. Nonferrous Met. Soc. China 25(2015) 249−260
Transactions of Nonferrous Metals Society of China
www.tnmsc.cn

Crystal anisotropy of AZ31 magnesium alloy under uniaxial tension and compression

Yong-ting LAN[1,2], Xian-ci ZHONG[3], Gao-feng QUAN[4], Ruo-cheng LIN[5], Ke-shi ZHANG[1]

1. Key Laboratory of Disaster Prevent and Structural Safety, Guangxi University, Nanning 530004, China;
2. School of Vocational & Technical Education, Guangxi University of Science & Technology, Liuzhou 545006, China;
3. College of Mathematics and Information Science, Guangxi University, Nanning 530004, China;
4. School of Materials Science and Engineering, Southwest Jiaotong University, Chengdu 610031, China;
5. College of Transportation Equipments and Ocean Engineering, Dalian Maritime University, Dalian 116026, China

Received 13 February 2014; accepted 12 June 2014

Abstract: To investigate the deformation twinning and the plastic anisotropy of the hexagonal-close-packed (HCP) single crystal, the crystal plastic constitutive model including slip and twinning deformation was established with finite element method based on crystal plasticity theory. The model was verified by test data. Newton−Raphson iteration method was developed with the stress components directly as the basic variables of iteration. The plastic deformation behavior of single crystal AZ31 alloy was analyzed numerically under monotonic tension and compression, respectively, in four different strain paths (i.e. along $\langle 2\bar{1}\bar{1}0\rangle$, $\langle 01\bar{1}0\rangle$, $\langle 0001\rangle$ and $\langle 01\bar{1}1\rangle$) with this model. The stress−strain curves were obtained in the above paths. The numerical calculation results show that this crystal model is feasible to predict the activity of slip/twinning system and to describe the number of active twin variants, the types of dominant twin variants and twin intersection. Due to the polar nature of mechanical twinning in inelastic deformation of the material, the plastic behavior of the single crystal material is demonstrated to be notably anisotropic and high asymmetry.

Key words: AZ31 magnesium alloy; constitutive model; single crystal; deformation twin; twin variant; twin intersection

1 Introduction

The magnesium alloys have recently been focused on because of their potential applications for lightweight structural parts [1,2]. However, a number of applications of magnesium alloys are set a limit because they always show a high anisotropy and are hard to deform at low homologous temperature [3], just their HCP structure and limited deformation models.

The closed packed directions for crystallographic slip on HCP crystals are $\langle 11\bar{2}0\rangle$ family of directions. Because these are perpendicular to the *c*-axis of the HCP crystals, they hardly cause the deformation along that axis. Twinning is considered to be one of the mechanisms that provide the inelastic deformation along the *c*-axis. In this regard, mechanical twinning plays a vital role in the deformation of magnesium alloy. At low homologous temperature, twinning may contribute this material to satisfy the von Mises criterion, which requires five independent deformation systems for meeting an arbitrary homogeneous straining. Unlike shear due to crystalline slip, the shear associated with twinning is typically polar in nature.

For the deformation of FCC and BCC materials which deform primarily by crystallographic slip, there has been already a well developed mathematical theory [4,5]. But the integration of deformation twinning as a mode of plastic deformation and crystallographic slip has been an unsolved problem in extending crystal plasticity models to a wider range of polycrystalline materials [6]. Investigators [7,8] have made a lot of efforts to study the plastic deformation of HCP crystal and have achieved fruitful results. A continuum approach [9] is presented for predicting the plastic behaviour of HCP polycrystals using a simple non-hardening constitutive model incorporating both slip and twinning. Although slip and twinning deformation are taken into account in

Foundation item: Projects (11272094, 11072064) supported by the National Natural Science Foundation of China; Project (LGZX201101) supported by the Laboratory Center of Guangxi Science and Technology, China; Project (1074023) supported by the Science Foundation of Guangxi University of Science & Technology, China
Corresponding author: Ke-shi ZHANG; Tel: +86-771-3275697; E-mail: zhangks@gxu.edu.cn
DOI: 10.1016/S1003-6326(15)63600-7

constitutive relation, the interaction between slip and twinning deformation has not been presented in the above literature. Meanwhile, the iterative solution of incremental constitutive equation still needs to be improved. To this end, a constitutive model including slip and twinning mechanism for polycrystalline HCP materials was established, in which the Newton−Raphson iteration algorithm with the stress components directly as the basic variables of iteration was proposed. This model took the interaction between slip dislocation and twinning dislocation into account and put forward the new hardening functions of slip and twinning deformation. It is first that the volume fraction of twinning is proposed as argument to hardening function of slip deformation. To examine the constitutive model and the algorithm for texture evolution, AZ31 magnesium alloy was studied. Then, meso-anisotropic nature of AZ31 single crystal was revealed by applying in different strain paths on single crystal. It is feasible to describing the activation of each deformation mechanism and twin variant during the single crystal deformation.

2 Slip and twinning deformation mechanism

The twinning can be regarded as a pseudo-slip. Then, the twinning plane and the correlative shear direction can be described by the normal of twinning plane vector and the shear direction vector, respectively. And they are integrated into the crystal plasticity model. Let α index the slip modes (i.e., prism or pyramidal) and β the twinning types. The power law is chosen to describe the shearing rates of the slip systems and extended to characterize the shearing rates of the twinning systems:

$$\dot{\gamma}_{\mathrm{S}}^{(\alpha)} = \dot{\gamma}_0 \operatorname{sgn}(\tau_{\mathrm{S}}^{(\alpha)}) \left| \frac{\tau_{\mathrm{S}}^{(\alpha)}}{g_{\mathrm{S}}^{(\alpha)}} \right|^k \tag{1a}$$

$$\dot{\gamma}_{\mathrm{T}}^{(\beta)} = \dot{\gamma}_0 \operatorname{sgn}(\tau_{\mathrm{T}}^{(\beta)}) \left(\frac{\tau_{\mathrm{T}}^{(\beta)}}{g_{\mathrm{T}}^{(\beta)}} \right)^k, \quad \tau_{\mathrm{T}}^{(\beta)} > 0 \tag{1b}$$

where $\dot{\gamma}_{\mathrm{S}}^{(\alpha)}$ and $\dot{\gamma}_{\mathrm{T}}^{(\beta)}$ denote the shear strain rates of slip systems and twinning system, respectively; $\tau_{\mathrm{S}}^{(\alpha)}$ and $\tau_{\mathrm{T}}^{(\beta)}$ denote the resolved shear stresses of slip plane and twin plane, respectively; $\dot{\gamma}_0$ is equivalent to the macroscopic strain rate modulus. This flow law introduces the critical strength or slip resistance $g_{\mathrm{S}}^{(\alpha)}$ that depends upon the local microstructure encountered by the dislocations; $g_{\mathrm{T}}^{(\beta)}$ denotes the thresholds demanded to activate this twin system; k is the rate-sensitivity parameter.

The pseudo-volume fraction of the twin due to twinning system β in each grain is defined by

$$f^{(\beta)} = \gamma_{\mathrm{T}}^{(\beta)} / \gamma_{\mathrm{twin}} \tag{2}$$

where $f^{(\beta)}$ denotes the volume fraction of twinning system β; $\gamma_{\mathrm{T}}^{(\beta)}$ is the accumulated shear strain of twinning system, calculated by $\gamma_{\mathrm{T}}^{(\beta)} = \left| \int \dot{\gamma}_{\mathrm{T}}^{(\beta)} \mathrm{d}t \right|$; γ_{twin} is the shear strain due to twinning system.

For compound twins, the orientation of a twin with respect to the matrix can be described by the rotation:

$$\boldsymbol{R}_{ij}^{\mathrm{tw}} = 2\boldsymbol{n}_i\boldsymbol{n}_j - \boldsymbol{\delta}_{ij} \tag{3}$$

where $\boldsymbol{R}_{ij}^{\mathrm{tw}}$ is the transformation matrix of orientation between twin and matrix; n is the twinning plane normal vector; δ_{ij} is the Kronecker delta. For later using, it is noted that in Miller−Bravais system, $\{\boldsymbol{a}_1, \boldsymbol{a}_2, \boldsymbol{a}_3, \boldsymbol{c}\}$, the four coordinate axes are not hard to numerical modeling, and the vectors $\boldsymbol{a}_1$, $\boldsymbol{a}_2$ and $\boldsymbol{a}_3$ are linearly dependent. For this reason, we define an orthonormal basis $\{x_M, M=1,2,3\}$ such that the x_1-axis is in the $\langle 2\bar{1}\bar{1}0 \rangle$ direction, x_2-axis is in the $\langle 01\bar{1}0 \rangle$ direction and the x_3-axis is in the $\langle 0001 \rangle$ direction (Fig. 1).

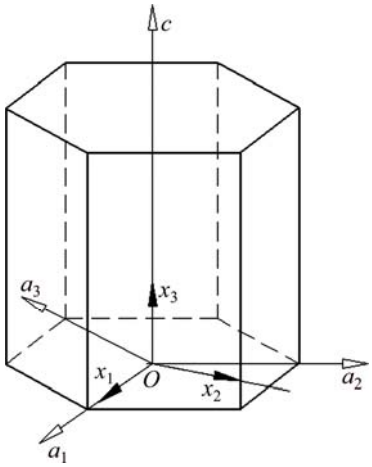

Fig. 1 Orthonormal system $\{x_M, M=1,2,3\}$ in unit cell

3 Constitutive equations

We adopt the original explanation provided by ASARO and RICE [10] for the multiplicative decomposition of deformation gradient, and extend the concepts of deformation gradient including deformation twinning:

$$\boldsymbol{F} = \boldsymbol{F}^{\mathrm{e}} \cdot \boldsymbol{F}^{\mathrm{p}} \tag{4}$$

where $\boldsymbol{F}$ is the total deformation gradient; $\boldsymbol{F}^{\mathrm{e}}$ contains deformation gradients owing to both elastic stretches and the lattice rotation; $\boldsymbol{F}^{\mathrm{p}}$ is the plastic deformation gradient.

It is assumed that the velocity gradient $\boldsymbol{L}$ consists of elastic velocity gradient $\boldsymbol{L}^{\mathrm{e}}$ and plastic velocity gradient $\boldsymbol{L}^{\mathrm{p}}$ in the current configuration:

$$\boldsymbol{L}=\boldsymbol{L}^{\mathrm{e}}+\boldsymbol{L}^{\mathrm{p}} \tag{5}$$

and the elastic velocity gradient $\boldsymbol{L}^{\mathrm{e}}$ is defined as

$$\boldsymbol{L}^{\mathrm{e}}=\dot{\boldsymbol{F}}^{\mathrm{e}}\cdot\boldsymbol{F}^{\mathrm{e}^{-1}} \tag{6}$$

with the superscript "·" denoting the derivative with respect to time, the superscript "−1" denoting the inverse of matrix. So, the plastic velocity gradient $\boldsymbol{L}^{\mathrm{p}}$ can be expressed as

$$\boldsymbol{L}^{\mathrm{p}}=\boldsymbol{F}^{\mathrm{e}}\cdot\dot{\boldsymbol{F}}^{\mathrm{p}}\cdot\boldsymbol{F}^{\mathrm{p}^{-1}}\cdot\boldsymbol{F}^{\mathrm{e}^{-1}} \tag{7}$$

Considering the slip and twinning mechanisms of plasticity, according to Ref. [11] we note that

$$\boldsymbol{L}^{\mathrm{p}}=\left(1-\sum_{\beta=1}^{N_{\mathrm{T}}}f^{\beta}\right)\sum_{\alpha=1}^{N_{\mathrm{S}}}\dot{\gamma}_{\mathrm{S}}^{(\alpha)}\boldsymbol{S}_{\mathrm{S}}^{(\alpha)}+\sum_{\beta=1}^{N_{\mathrm{T}}}\dot{\gamma}_{\mathrm{T}}^{(\beta)}\boldsymbol{S}_{\mathrm{T}}^{(\beta)}+\sum_{\beta=1}^{N_{\mathrm{T}}}\left(f^{\beta}\sum_{\alpha=1}^{N_{\mathrm{ST}}}\dot{\gamma}_{\mathrm{ST}}^{(\alpha)}\boldsymbol{S}_{\mathrm{ST}}^{(\alpha)}\right) \tag{8}$$

where $\dot{\gamma}_{\mathrm{S}}^{(\alpha)}$ and $\dot{\gamma}_{\mathrm{ST}}^{(\alpha)}$ denote the shear rate on a slip system in the untwinned crystal and in the twinned regions of the crystal, respectively; $\dot{\gamma}_{\mathrm{T}}^{(\beta)}$ denotes the shear strain related to twinning; f^{β} is the volume fraction of the twinned region; N_{S}, N_{T} and N_{ST} refer to the number of potentially active slip systems in the untwinned crystal, the number of potentially active twin systems in the untwinned crystal, and the number of potentially active slip systems in each of the twinned regions of the crystal, respectively; $\boldsymbol{S}_{\mathrm{S}}^{(\alpha)}$ represents the slip systems in the untwinned crystal; $\boldsymbol{S}_{\mathrm{T}}^{(\beta)}$ stands for the potential twin systems in the untwinned crystal; $\boldsymbol{S}_{\mathrm{ST}}^{(\alpha)}$ stands for the potential slip systems in the twinned areas of the crystal. Here,

$$\begin{cases}\boldsymbol{S}_{\mathrm{S}}=\boldsymbol{m}_{\mathrm{S}}^{*}\boldsymbol{n}_{\mathrm{S}}^{*}\\ \boldsymbol{S}_{\mathrm{T}}=\boldsymbol{m}_{\mathrm{T}}^{*}\boldsymbol{n}_{\mathrm{T}}^{*}\\ \boldsymbol{S}_{\mathrm{ST}}=\boldsymbol{m}_{\mathrm{ST}}^{*}\boldsymbol{n}_{\mathrm{ST}}^{*}\end{cases} \tag{9}$$

with

$$\begin{cases}\boldsymbol{m}_{\mathrm{S}}^{*}=\boldsymbol{F}^{\mathrm{e}}\cdot\boldsymbol{m}_{0\_\mathrm{S}},\quad \boldsymbol{n}_{\mathrm{S}}^{*}=\boldsymbol{F}^{\mathrm{e}^{-\mathrm{T}}}\cdot\boldsymbol{n}_{0\_\mathrm{S}}\\ \boldsymbol{m}_{\mathrm{T}}^{*}=\boldsymbol{F}^{\mathrm{e}}\cdot\boldsymbol{m}_{0\_\mathrm{T}},\quad \boldsymbol{n}_{\mathrm{T}}^{*}=\boldsymbol{F}^{\mathrm{e}^{-\mathrm{T}}}\cdot\boldsymbol{n}_{0\_\mathrm{T}}\\ \boldsymbol{m}_{\mathrm{ST}}^{*}=\boldsymbol{R}^{\mathrm{TW}}\cdot(\boldsymbol{F}^{\mathrm{e}}\cdot\boldsymbol{m}_{0\_\mathrm{S}})\\ \boldsymbol{n}_{\mathrm{ST}}^{*}=\boldsymbol{R}^{\mathrm{TW}}\cdot(\boldsymbol{F}^{\mathrm{e}^{-\mathrm{T}}}\cdot\boldsymbol{n}_{0\_\mathrm{S}})\end{cases} \tag{10}$$

where superscript "T" denotes the transpose of the matrix. Note that each system is specified by a unit normal $\boldsymbol{n}_0$ to the slip/twin plane, and a unit vector $\boldsymbol{m}_0$ denoting the slip/twin direction. The slip and twin systems ($\boldsymbol{n}_0$, $\boldsymbol{m}_0$) are supposed to be known in the reference configuration.

The plastic deformation rate tensor $\boldsymbol{D}^{\mathrm{p}}$ and plastic spin tensor $\boldsymbol{W}^{\mathrm{p}}$ are defined as

$$\boldsymbol{D}^{\mathrm{p}}=\frac{1}{2}(\boldsymbol{L}^{\mathrm{p}}+\boldsymbol{L}^{\mathrm{p}^{\mathrm{T}}}) \tag{11a}$$

$$\boldsymbol{W}^{\mathrm{p}}=\frac{1}{2}(\boldsymbol{L}^{\mathrm{p}}-\boldsymbol{L}^{\mathrm{p}^{\mathrm{T}}}) \tag{11b}$$

and

$$\boldsymbol{L}^{\mathrm{p}}=\boldsymbol{D}^{\mathrm{p}}+\boldsymbol{W}^{\mathrm{p}} \tag{12}$$

3.1 Time-integration scheme

With reference to the specific spatial coordinate x_M concentric with the current local crystallographic axes, the incremental formulation can be written as

$$\Delta\boldsymbol{\sigma}_M=\boldsymbol{C}_M:\Delta\boldsymbol{\varepsilon}_M^{\mathrm{e}} \tag{13}$$

where $\Delta\boldsymbol{\sigma}_M$ and $\Delta\boldsymbol{\varepsilon}_M^{\mathrm{e}}$ denote the Cauchy stress increment and the elastic strain increment with reference to x_M, respectively; $\boldsymbol{C}_M$ denotes the 4th-order tensor of tangent elasticity of the material with reference to x_M.

The stresses in the twinned and untwinned areas of the crystal can be described as

$$\begin{cases}\boldsymbol{\sigma}_M^{\mathrm{mt}}=\boldsymbol{C}_M^{\mathrm{mt}}:\boldsymbol{\varepsilon}_M^{\mathrm{e}}\\ \boldsymbol{\sigma}_M^{\mathrm{tw}}=\boldsymbol{C}_M^{\mathrm{tw}}:\boldsymbol{\varepsilon}_M^{\mathrm{e}}\end{cases} \tag{14}$$

where superscripts "mt" and "tw" denote the untwinned and the twinned regions, respectively. Note that different elastic stiffness tensors are used in Eq. (14) for the parents and the twinned areas, for the sake of the differences in the lattice orientations in these areas in the intermediate configuration. In addition, $\boldsymbol{C}_M^{\mathrm{mt}}$ can be related to $\boldsymbol{C}_M^{\mathrm{tw}}$ by the transformation:

$$\boldsymbol{C}_{Mijkl}^{\mathrm{tw}}=\boldsymbol{C}_{Mpqrs}^{\mathrm{mt}}R_{ip}^{\mathrm{tw}}R_{jq}^{\mathrm{tw}}R_{kr}^{\mathrm{tw}}R_{ts}^{\mathrm{tw}} \tag{15}$$

The Cauchy stress increment in a crystal is expressed as a volume average of the stresses in the parents and the twinned regions, i.e.

$$\Delta\boldsymbol{\sigma}_M=\left(1-\sum_{\beta}f^{\beta}\right)\Delta\boldsymbol{\sigma}_M^{\mathrm{mt}}+\sum_{\beta}f^{\beta}\Delta\boldsymbol{\sigma}_M^{\mathrm{tw}\beta} \tag{16}$$

where f^{β} is the volume fraction of the grain that is twinned to the β twin system; $\Delta\boldsymbol{\sigma}_M^{\mathrm{tw}\beta}$ denotes the Cauchy stress increment in the β twinned region.

Combining Eqs. (13), (14) and (16), we have

$$\Delta\boldsymbol{\sigma}_M=\left\{\left(1-\sum_{\beta}f^{\beta}\right)\boldsymbol{C}_M^{\mathrm{mt}}+\sum_{\beta}f^{\beta}\boldsymbol{C}_M^{\mathrm{tw}\beta}\right\}:\Delta\boldsymbol{\varepsilon}_M^{\mathrm{e}} \tag{17}$$

and

$$\boldsymbol{C}_M=\left(1-\sum_{\beta}f^{\beta}\right)\boldsymbol{C}_M^{\mathrm{mt}}+\sum_{\beta}f^{\beta}\boldsymbol{C}_M^{\mathrm{tw}\beta} \tag{18}$$

Further, it is assumed that $\Delta\boldsymbol{\varepsilon}_M$ can be expressed as the sum of $\Delta\boldsymbol{\varepsilon}_M^{\mathrm{e}}$ and $\Delta\boldsymbol{\varepsilon}_M^{\mathrm{p}}$:

$$\Delta\boldsymbol{\varepsilon}_M=\Delta\boldsymbol{\varepsilon}_M^{\mathrm{e}}+\Delta\boldsymbol{\varepsilon}_M^{\mathrm{p}} \tag{19}$$

In the constitutive model of crystal plasticity, a rate

formulation is used and dislocation motions on multiple slipping and twin systems are considered. The flow law controlling the rate of plastic strain of a single crystal is

$$\Delta\boldsymbol{\varepsilon}_M^{\mathrm{p}}=\boldsymbol{D}^{\mathrm{p}}\Delta t=\left(1-\sum_{\beta=1}^{N_{\mathrm{T}}}f^{\beta}\right)\sum_{\alpha=1}^{N_{\mathrm{S}}}\boldsymbol{P}_{\mathrm{S}}^{(\alpha)}\Delta\gamma_{\mathrm{S}}^{(\alpha)}+\sum_{\beta=1}^{N_{\mathrm{T}}}\boldsymbol{P}_{\mathrm{T}}^{(\beta)}\Delta\gamma_{\mathrm{T}}^{(\beta)}+\sum_{\beta=1}^{N_{\mathrm{T}}}\left(f^{\beta}\sum_{\alpha=1}^{N_{\mathrm{ST}}}\boldsymbol{P}_{\mathrm{ST}}^{(\alpha)}\Delta\gamma_{\mathrm{ST}}^{(\alpha)}\right) \tag{20}$$

where $\boldsymbol{P}=\frac{1}{2}(\boldsymbol{m}^{*}\boldsymbol{n}^{*}+\boldsymbol{n}^{*}\boldsymbol{m}^{*})$ is termed the Schmid direction tensor with reference to x_M.

For convenience, hereafter the quantity calculation is related to the configurations before and after a small time discretization step Δt with the left superscripts t and $t+\Delta t$, respectively. Usually, for meeting the objectivity of the stress, the update of stress is calculated as follows [12]:

$${}^{t+\Delta t}\boldsymbol{\sigma}_M={}^{t}\boldsymbol{\sigma}_M+\boldsymbol{C}_M:(\Delta\boldsymbol{\varepsilon}_M-\Delta\boldsymbol{\varepsilon}_M^{\mathrm{p}}) \tag{21}$$

Applying Eq. (20) into Eq. (21) gives

$${}^{t+\Delta t}\boldsymbol{\sigma}_M={}^{t}\boldsymbol{\sigma}_M+\boldsymbol{C}_M:\Delta\boldsymbol{\varepsilon}_M-\boldsymbol{C}_M:\left[\left(1-\sum_{\beta=1}^{N_{\mathrm{T}}}f^{\beta}\right)\sum_{\alpha=1}^{N_{\mathrm{S}}}\boldsymbol{P}_{\mathrm{S}}^{(\alpha)}\Delta\gamma_{\mathrm{S}}^{(\alpha)}+\sum_{\beta=1}^{N_{\mathrm{T}}}\boldsymbol{P}_{\mathrm{T}}^{(\beta)}\Delta\gamma_{\mathrm{T}}^{(\beta)}+\sum_{\beta=1}^{N_{\mathrm{T}}}\left(f^{\beta}\sum_{\alpha=1}^{N_{\mathrm{ST}}}\boldsymbol{P}_{\mathrm{ST}}^{(\alpha)}\Delta\gamma_{\mathrm{ST}}^{(\alpha)}\right)\right] \tag{22}$$

The value of $\Delta\gamma$ can be calculated by

$$\Delta\gamma=\left[(1-\eta)\,{}^{t}\dot{\gamma}+\eta\,{}^{t+\Delta t}\dot{\gamma}\right]\Delta t \tag{23}$$

with η being a parameter limited in the range of $0<\eta<1$. And

$$\begin{cases}{}^{t}\dot{\gamma}_{\mathrm{S}}^{(\alpha)}=\dot{\gamma}_0\,\mathrm{sgn}({}^{t}\tau_{\mathrm{S}}^{(\alpha)})\left|\dfrac{{}^{t}\tau_{\mathrm{S}}^{(\alpha)}}{{}^{t}g_{\mathrm{S}}^{(\alpha)}}\right|^{k}\\ {}^{t+\Delta t}\dot{\gamma}_{\mathrm{S}}^{(\alpha)}=\dot{\gamma}_0\,\mathrm{sgn}({}^{t+\Delta t}\tau_{\mathrm{S}}^{(\alpha)})\left|\dfrac{{}^{t+\Delta t}\tau_{\mathrm{S}}^{(\alpha)}}{{}^{t+\Delta t}g_{\mathrm{S}}^{(\alpha)}}\right|^{k}\end{cases} \tag{24a}$$

$$\begin{cases}{}^{t}\dot{\gamma}_{\mathrm{T}}^{(\beta)}=\dot{\gamma}_0\,\mathrm{sgn}({}^{t}\tau_{\mathrm{T}}^{(\beta)})\left(\dfrac{{}^{t}\tau_{\mathrm{T}}^{(\beta)}}{{}^{t}g_{\mathrm{T}}^{(\beta)}}\right)^{k}\\ {}^{t+\Delta t}\dot{\gamma}_{\mathrm{T}}^{(\beta)}=\dot{\gamma}_0\,\mathrm{sgn}({}^{t+\Delta t}\tau_{\mathrm{T}}^{(\beta)})\left(\dfrac{{}^{t+\Delta t}\tau_{\mathrm{T}}^{(\beta)}}{{}^{t+\Delta t}g_{\mathrm{T}}^{(\beta)}}\right)^{k}\end{cases} \tag{24b}$$

$$\begin{cases}{}^{t}\dot{\gamma}_{\mathrm{ST}}^{(\alpha)}=\dot{\gamma}_0\,\mathrm{sgn}({}^{t}\tau_{\mathrm{ST}}^{(\alpha)})\left|\dfrac{{}^{t}\tau_{\mathrm{ST}}^{(\alpha)}}{{}^{t}g_{\mathrm{ST}}^{(\alpha)}}\right|^{k}\\ {}^{t+\Delta t}\dot{\gamma}_{\mathrm{ST}}^{(\alpha)}=\dot{\gamma}_0\,\mathrm{sgn}({}^{t+\Delta t}\tau_{\mathrm{ST}}^{(\alpha)})\left|\dfrac{{}^{t+\Delta t}\tau_{\mathrm{ST}}^{(\alpha)}}{{}^{t+\Delta t}g_{\mathrm{ST}}^{(\alpha)}}\right|^{k}\end{cases} \tag{24c}$$

Substituting Eqs. (23) and (24) into Eq. (22), we have

$${}^{t+\Delta t}\boldsymbol{\sigma}_M={}^{t}\boldsymbol{\sigma}_M+\left\{\boldsymbol{C}_M:\left(\Delta\boldsymbol{\varepsilon}_M-(1-\eta)\Delta t\left(\left(1-\sum_{\beta=1}^{N_{\mathrm{T}}}f^{\beta}\right)\sum_{\alpha=1}^{N_{\mathrm{S}}}\boldsymbol{P}_{\mathrm{S}}^{(\alpha)}\,{}^{t}\dot{\gamma}_{\mathrm{S}}^{(\alpha)}+\sum_{\beta=1}^{N_{\mathrm{T}}}\boldsymbol{P}_{\mathrm{T}}^{(\beta)}\,{}^{t}\dot{\gamma}_{\mathrm{T}}^{(\beta)}+\sum_{\beta=1}^{N_{\mathrm{T}}}f^{\beta}\sum_{\alpha=1}^{N_{\mathrm{ST}}}\boldsymbol{P}_{\mathrm{ST}}^{(\alpha)}\,{}^{t}\dot{\gamma}_{\mathrm{ST}}^{(\alpha)}\right)\right)\right\}-\eta\Delta t\dot{\gamma}_0\left\{\boldsymbol{C}_M:\left(\left(1-\sum_{\beta=1}^{N_{\mathrm{T}}}f^{\beta}\right)\sum_{\alpha=1}^{N_{\mathrm{S}}}\boldsymbol{P}_{\mathrm{S}}^{(\alpha)}\,{}^{t+\Delta t}\dot{\gamma}_{\mathrm{S}}^{(\alpha)}+\sum_{\beta=1}^{N_{\mathrm{T}}}\boldsymbol{P}_{\mathrm{T}}^{(\beta)}\,{}^{t+\Delta t}\dot{\gamma}_{\mathrm{T}}^{(\beta)}+\sum_{\beta=1}^{N_{\mathrm{T}}}f^{\beta}\sum_{\alpha=1}^{N_{\mathrm{ST}}}\boldsymbol{P}_{\mathrm{ST}}^{(\alpha)}\,{}^{t+\Delta t}\dot{\gamma}_{\mathrm{ST}}^{(\alpha)}\right)\right\} \tag{25}$$

with

$${}^{t+\Delta t}\dot{\gamma}_{\mathrm{S}}^{(\alpha)}=\mathrm{sgn}(\boldsymbol{P}_{\mathrm{S}}^{(\alpha)}:{}^{t+\Delta t}\boldsymbol{\sigma}_M)\left(\frac{\left|\boldsymbol{P}_{\mathrm{S}}^{(\alpha)}:{}^{t+\Delta t}\boldsymbol{\sigma}_M\right|}{{}^{t+\Delta t}g_{\mathrm{S}}^{(\alpha)}}\right)^{k} \tag{26a}$$

$${}^{t+\Delta t}\dot{\gamma}_{\mathrm{T}}^{(\beta)}=\mathrm{sgn}(\boldsymbol{P}_{\mathrm{T}}^{(\beta)}:{}^{t+\Delta t}\boldsymbol{\sigma}_M)\left(\frac{\boldsymbol{P}_{\mathrm{T}}^{(\beta)}:{}^{t+\Delta t}\boldsymbol{\sigma}_M}{{}^{t+\Delta t}g_{\mathrm{T}}^{(\beta)}}\right)^{k} \tag{26b}$$

$${}^{t+\Delta t}\dot{\gamma}_{\mathrm{ST}}^{(\alpha)}=\mathrm{sgn}(\boldsymbol{P}_{\mathrm{ST}}^{(\alpha)}:{}^{t+\Delta t}\boldsymbol{\sigma}_M)\left(\frac{\left|\boldsymbol{P}_{\mathrm{ST}}^{(\alpha)}:{}^{t+\Delta t}\boldsymbol{\sigma}_M\right|}{{}^{t+\Delta t}g_{\mathrm{ST}}^{(\alpha)}}\right)^{k} \tag{26c}$$

3.2 Stress-based Newton−Raphson iteration method

For the convenience of implementing the algorithms in an ABAQUS/Standard code, we rewrite Eq. (25) in the form

$$\boldsymbol{F}({}^{t+\Delta t}\boldsymbol{\sigma}_M)={}^{t+\Delta t}\boldsymbol{\sigma}_M+\boldsymbol{H}({}^{t+\Delta t}\boldsymbol{\sigma}_M)-\boldsymbol{r}=0 \tag{27}$$

with

$$\boldsymbol{H}({}^{t+\Delta t}\boldsymbol{\sigma}_M)=\eta\Delta t\dot{\gamma}_0\left[\boldsymbol{C}_M:\boldsymbol{H}_1({}^{t+\Delta t}\boldsymbol{\sigma}_M)\right] \tag{28}$$

$$\boldsymbol{H}_1({}^{t+\Delta t}\boldsymbol{\sigma}_M)=\left(\left(1-\sum_{\beta=1}^{N_{\mathrm{T}}}f^{\beta}\right)\sum_{\alpha=1}^{N_{\mathrm{S}}}\boldsymbol{P}_{\mathrm{S}}^{(\alpha)}\,{}^{t+\Delta t}\dot{\gamma}_{\mathrm{S}}^{(\alpha)}+\sum_{\beta=1}^{N_{\mathrm{T}}}\boldsymbol{P}_{\mathrm{T}}^{(\beta)}\,{}^{t+\Delta t}\dot{\gamma}_{\mathrm{T}}^{(\beta)}+\sum_{\beta=1}^{N_{\mathrm{T}}}f^{\beta}\sum_{\alpha=1}^{N_{\mathrm{ST}}}\boldsymbol{P}_{\mathrm{ST}}^{(\alpha)}\,{}^{t+\Delta t}\dot{\gamma}_{\mathrm{ST}}^{(\alpha)}\right) \tag{29}$$

and

$$\boldsymbol{r}={}^{t}\boldsymbol{\sigma}_M+\left\{\boldsymbol{C}_M:(\Delta\boldsymbol{\varepsilon}_M-(1-\eta)\Delta t\left(\left(1-\sum_{\beta=1}^{N_{\mathrm{T}}}f^{\beta}\right)\sum_{\alpha=1}^{N_{\mathrm{S}}}\boldsymbol{P}_{\mathrm{S}}^{(\alpha)}\,{}^{t}\dot{\gamma}_{\mathrm{S}}^{(\alpha)}+\sum_{\beta=1}^{N_{\mathrm{T}}}\boldsymbol{P}_{\mathrm{T}}^{(\beta)}\,{}^{t}\dot{\gamma}_{\mathrm{T}}^{(\beta)}+\right.\right.$$

$$\sum_{\beta=1}^{N_T} f^{\beta} \sum_{\alpha=1}^{N_{ST}} \boldsymbol{P}_{ST}^{(\alpha)}\, {}^{t}\dot{\gamma}_{ST}^{(\alpha)} \Bigg)\Bigg)\Bigg\} \tag{30}$$

Then, the stress-based Newton−Raphson iteration can be therefore written as

$$\boldsymbol{F}({}^{t+\Delta t}\boldsymbol{\sigma}_M) + \frac{\partial \boldsymbol{F}}{\partial({}^{t+\Delta t}\boldsymbol{\sigma}_M)} \cdot \boldsymbol{\delta}({}^{t+\Delta t}\boldsymbol{\sigma}_M) = 0 \tag{31}$$

with

$$\boldsymbol{F}({}^{t+\Delta t}\boldsymbol{\sigma}_M) = {}^{t+\Delta t}\boldsymbol{\sigma}_M + \boldsymbol{H}({}^{t+\Delta t}\boldsymbol{\sigma}_M) - \boldsymbol{r} \tag{32}$$

and

$$\frac{\partial \boldsymbol{F}}{\partial({}^{t+\Delta t}\boldsymbol{\sigma})} = \boldsymbol{I} + \boldsymbol{C}_M :$$

$$\left(\left(1 - \sum_{\beta=1}^{N_T} f^{\beta}\right) \sum_{\alpha=1}^{N_S} \frac{k}{g_S^{(\alpha)}} \left| \frac{\boldsymbol{P}_S^{(\alpha)} : {}^{t+\Delta t}\boldsymbol{\sigma}_M}{g_S^{(\alpha)}} \right|^{k-1} \boldsymbol{P}_S^{(\alpha)} \boldsymbol{P}_S^{(\alpha)} + \right.$$

$$\sum_{\alpha=1}^{N_T} \frac{k}{g_T^{(\beta)}} \left(\frac{\boldsymbol{P}_T^{(\beta)} : {}^{t+\Delta t}\boldsymbol{\sigma}_M}{g_T^{(\beta)}} \right)^{k-1} \boldsymbol{P}_T^{(\beta)} \boldsymbol{P}_T^{(\beta)} +$$

$$\left. \sum_{\beta=1}^{N_T} \left(f^{\beta} \sum_{\alpha=1}^{N_{ST}} \frac{k}{g_{ST}^{(\alpha)}} \left| \frac{\boldsymbol{P}_{ST}^{(\alpha)} : {}^{t+\Delta t}\boldsymbol{\sigma}_M}{g_{ST}^{(\alpha)}} \right|^{k-1} \boldsymbol{P}_{ST}^{(\alpha)} \boldsymbol{P}_{ST}^{(\alpha)} \right) \right) \eta \Delta t \dot{\gamma}_0 \tag{33}$$

where $\boldsymbol{\delta}({}^{t+\Delta t}\boldsymbol{\sigma}_M)$ is the stress variation for the iteration, and $\boldsymbol{I}$ is the identity tensor.

3.3 Deformation mechanism and hardening function

According the results in Ref. [13], in the numerical study represented below, the operative slip and twin systems are supposed to be the slip on basal $\langle a \rangle$ (0001) $\langle 11\bar{2}0 \rangle$, prismatic $\langle a \rangle (1\bar{1}00)$ $\langle 11\bar{2}0 \rangle$, pyramidal $\langle a+c \rangle$ $(2\bar{1}\bar{1}2)$ $\langle \bar{2}113 \rangle$ systems and twinning on pyramidal $(1\bar{1}02)$ $\langle \bar{1}101 \rangle$ and $(1\bar{1}01)$ $\langle 1\bar{1}02 \rangle$ systems.

There are 12 slip systems and 12 twin systems for a HCP single crystal of AZ31. The normal vector n_0 and the slip direction vector m_0 corresponding to each slip/twin plane are given in Tables 1 and 2.

Table 1 Labels of direction and plane of slip systems for AZ31 single crystal

Slip No.	n_0		m_0	
	a	*b*	*a*	*b*
1	(0001)	(001)	$\langle 11\bar{2}0 \rangle$	⟨0.5,0.886,0⟩
2	(0001)	(001)	$\langle 1\bar{2}10 \rangle$	⟨0.5,−0.866,0⟩
3	(0001)	(001)	$\langle \bar{2}110 \rangle$	⟨−1,0,0⟩
4	$(1\bar{1}00)$	(0.866,−0.5,0)	$\langle 11\bar{2}0 \rangle$	⟨0.5,0.866,0⟩
5	$(\bar{1}010)$	(−0.866,−0.5,0)	$\langle 1\bar{2}10 \rangle$	⟨0.5,−0.866,0⟩
6	$(01\bar{1}0)$	(0,1,0)	$\langle \bar{2}110 \rangle$	⟨−1,0,0⟩
7	$(2\bar{1}\bar{1}2)$	(0.852,0,0.524)	$\langle \bar{2}113 \rangle$	⟨−0.524,0,0.852⟩
8	$(\bar{1}\bar{1}22)$	(−0.426,−0.737,0.524)	$\langle 11\bar{2}3 \rangle$	⟨0.262,0.454,0.852⟩
9	$(\bar{1}2\bar{1}2)$	(−0.426,0.737,0.524)	$\langle 1\bar{2}13 \rangle$	⟨0.262,−0.454,0.852⟩
10	$(\bar{2}112)$	(−0.852,0,0.524)	$\langle 2\bar{1}\bar{1}3 \rangle$	⟨0.524,0,0.852⟩
11	$(11\bar{2}2)$	(0.426,0.737,0.524)	$\langle \bar{1}\bar{1}23 \rangle$	⟨−0.262,0.454,0.852⟩
12	$(1\bar{2}12)$	(0.426,−0.737,0.524)	$\langle \bar{1}2\bar{1}3 \rangle$	⟨−0.262,0.454,0.852⟩

a—Four axis coordinate in Miller−Bravais system; *b*—Cartesian coordinate in $\{x_M, M=1,2,3\}$.

Table 2 Labels of direction and plane of twinning systems for AZ31 single crystal

Twinning No.	n_0		m_0	
	a	*b*	*a*	*b*
1	$(1\bar{1}02)$	(0.592,−0.342,0.729)	$\langle \bar{1}101 \rangle$	⟨−0.632,0.365,0.684⟩
2	$(\bar{1}012)$	(−0.592,−0.342,0.729)	$\langle 10\bar{1}1 \rangle$	⟨0.632,0.365,0.684⟩
3	$(01\bar{1}2)$	(0,0.684,0.729)	$\langle 0\bar{1}11 \rangle$	⟨0,−0.729,0.684⟩
4	$(\bar{1}102)$	(−0.592,0.342,0.729)	$\langle 1\bar{1}01 \rangle$	⟨0.632,−0.365,0.684⟩
5	$(10\bar{1}2)$	(0.592,0.342,0.729)	$\langle \bar{1}011 \rangle$	⟨−0.632,−0.365,0.684⟩
6	$(0\bar{1}12)$	(0,−0.684,0.729)	$\langle 01\bar{1}1 \rangle$	⟨0,0.729,0.684⟩
7	$(1\bar{1}01)$	(0.764,−0.441,0.471)	$\langle 1\bar{1}02 \rangle$	⟨0.408,−0.235,−0.882⟩
8	$(\bar{1}011)$	(−0.764,−0.441,0.471)	$\langle \bar{1}01\bar{2} \rangle$	⟨−0.408,−0.235,−0.882⟩
9	$(01\bar{1}1)$	(0,0.882,0.471)	$\langle 01\bar{1}\bar{2} \rangle$	⟨0,0.471,−0.882⟩
10	$(\bar{1}101)$	(−0.764,0.441,0.471)	$\langle \bar{1}10\bar{2} \rangle$	⟨−0.408,0.235,−0.882⟩
11	$(10\bar{1}1)$	(0.764,0.441,0.471)	$\langle 10\bar{1}\bar{2} \rangle$	⟨0.408,0.235,−0.882⟩
12	$(0\bar{1}11)$	(0,−0.882,0.471)	$\langle 0\bar{1}1\bar{2} \rangle$	⟨0,−0.471,−0.882⟩

Depending on the family of slip/twin systems, the evolution rule for the hardening $g^{(\alpha)}$ is expressed as [14]

$$\dot{g}^{(\alpha)}=\sum_{\beta=1}^{n}h_{\alpha\beta}\left|\dot{\gamma}^{(\beta)}\right| \tag{34}$$

where $h_{\alpha\beta}$ is the slip/twin hardening modulus and is proposed as

$$h_{\alpha\beta}(\gamma)=h(\gamma)\left[q+(1-q)\delta_{\alpha\beta}\right] \tag{35}$$

where q is a constant. Hardening parameter $h(\gamma)$ and the values of the coupling parameter q have to be calibrated by a fitting procedure accounting for the test results of the polycrystal.

Since twin boundaries (TB) impede the motion of slip dislocation after twinning in the grain to some extent, the hardening of slip deformation is closely associated with twin boundaries or the volume fraction of twin. In addition, the slip dislocation can penetrate into the twin. So Hall−Petch effect due to twinning is weakened. The experiments presented in Ref. [15] show that there are visible differences between the slip hardening rates with twin and without twin. Obviously, these differences depend on the volume fraction of twin. Based on the above analysis, the slip hardening modulus $h_s(\gamma)$ is applied as follows:

$$h_S(\gamma)=h_0\mathrm{sech}^2\left(\frac{h_0\gamma}{(\tau_s-\tau_0)\mathrm{e}^{rf}}\right) \tag{36}$$

where γ is the accumulated shear strain of all slip systems, and $\gamma=\int\sum_{\alpha=1}^{n}\left|\mathrm{d}\gamma^{(\alpha)}\right|$; h_0 is the initial hardening value; τ_0 and τ_s are the shear stresses at the onset of yield and the saturation of hardening, respectively. Note that τ_0 is used as the initial value of $g^{(\alpha)}$, namely, the critical resolved shear stress(CRSS); f denotes the volume fraction of twin, and $f=\sum f^{(\beta)}$; r is a coupling parameter determined by fitting the experimental data.

Experiments [16] indicate that the slip dislocations do not impede twinning deformation and the twin hardening rate keeps in a zero state or softening occurs within a narrow range with the increase of strain at the beginning stage of twinning deformation, and does not start to grow until the strain reaches about 3%, and increases rapidly as the following increase of strain. When the strain reaches about 6.5%, the twin hardening rate becomes so high that the twinning deformation hardly occurs, namely twinning exhausted phenomenon. In view of the above hardening evolution, the twin hardening modulus $h_T(\gamma)$ is applied as follows:

$$h_T(\gamma)=h_0\left(\cosh^2\left(\frac{h_0\gamma}{\tau_s-\tau_0}\right)-1\right) \tag{37}$$

where γ is the accumulated shear strain of all twinning systems, and $\gamma=\int\sum_{\beta=1}^{n}\left|\mathrm{d}\gamma^{(\beta)}\right|$.

4 Numerical results

Figure 2 shows the schematic of the finite element model. The cubic model is divided into seven uniform parts in each direction, and eight-node iso-parametric brick elements with reduced integration are adopted. Initial crystal orientations for all elements are arranged randomly. Thus, the number of initial crystal orientations of the model is 7×7×7=343.

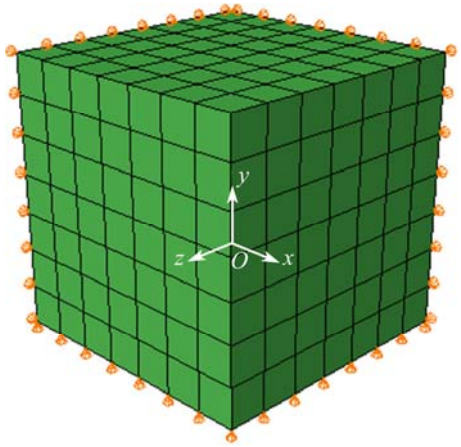

Fig. 2 Schematic of finite element analysis model

4.1 Validation of constitutive model and stress−strain response for AZ31 magnesium sheet

Based on test data by MARKO et al [17], the initial (0001) and $(10\bar{1}0)$ pole figures of the model are shown in Fig. 3. In the calculation, the *x*-, *y*-, and *z*-axes in Fig. 2 are defined to be the rolling direction (RD), transverse direction (TD), and normal direction (ND) in the sheet, respectively. Thus, the majority of *c*-axis is tended to align in the *z* direction (ND). All calculations are performed by adopting the boundary conditions in Fig. 2 to predict the strength differential effect of uniaxial tension and compression, i.e., the planes x=0, y=0, and z=0 are fixed in the *x*, *y*, and *z* directions, respectively. For uniaxial tension, the plane y=1 is extended at a fixed

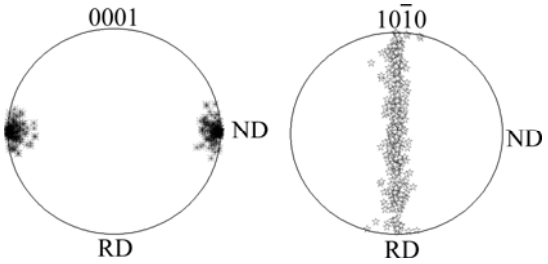

Fig. 3 Pole figures showing initial texture in analysis models

displacement rate, while for uniaxial compression it is compressed at a constant displacement rate.

The material parameters of the crystal model are estimated from the macroscopic stress−strain curve through tracking the experiments, via the trial-and-error method to fit the computationally obtained curves by applying a specified load on finite element model (Fig. 2). Due to the variation in microstructures, there are large discrepancies in the material parameters of magnesium alloy made by various processing technologies, especially CRSS, for example. In general, the reasonableness of the material parameters estimated numerically can be judged by comparing with the experiments, through verifying the reflection of texture evolution and macroscopic stress−strain curve of the simulation. The result of stress−strain curve is compared with the experimental result reported in Ref. [17]. And there is an attempt to match the stress−strain response with experimental results. A set of material parameters that give an acceptable matching to the stress−strain curve are given in Table 3.

Table 3 Model hardening parameters of AZ31 single crystal

Deformation modes	τ_0/ MPa	τ_s/ MPa	h_0/ MPa	γ_0/ s^{-1}	q	r	k
Basal-⟨a⟩	10	20	100	0.001	1.4	2.2	200
Prismatic-⟨a⟩	75	105	250	0.001	1.4	2.2	200
Pyramical-⟨a+c⟩	90	110	250	0.001	1.4	2.2	200
Tensile-twin	50	145	500	0.001	1.4	−	200
Compression-twin	100	155	500	0.001	1.4	−	200

The quite similar stress−strain curves shown in Fig. 4 can be obtained by this set of hardening parameters. It indicates that the stress−strain curves under uniaxial tension and compression obtained by this set of hardening parameters are in good accordance qualitatively with the test results by MARKO et al [17].

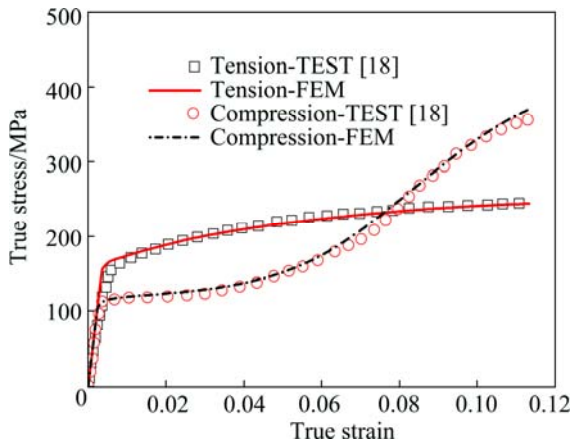

Fig. 4 Stress−strain curves under uniaxial tension and compression

Therefore, we consider that the following discussion about the activities of the slip and twinning systems is acceptable with regard to the set of hardening parameters.

4.2 Calculation of texture evolution for AZ31 magnesium alloy

Figure 5 shows the initial random texture in (0001) pole figure in terms of 343 grains for the AZ31 polycrystal at ε=0. The homogeneous deformation is considered by plane strain compression.

The predicted stress−strain curves and deformed textures at ε=0.1 and ε=0.2 are also shown in Fig. 5. The predicted results reveal that the textures in (0001) pole figure gradually result in the textures that the c-axis of most grains is approximately parallel to the direction of compression from initial random textures during compression process. Here, the predicted textures are essentially in accordance with basal plane textures of the rolled magnesium alloy sheet [19].

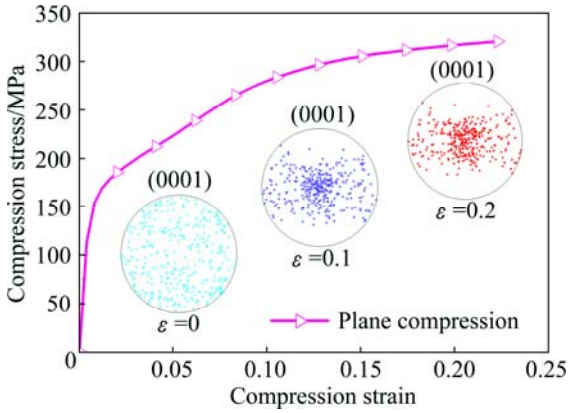

Fig. 5 Predicted stress−strain curve and textures evolution under plane strain compression for HCP polycrystal

5 Discussion

To investigate the whole behavior of the single crystal, we computed the response of the single crystal under uniaxial tension and compressions in four different directions: 1) ⟨$2\bar{1}\bar{1}0$⟩, 2) ⟨$01\bar{1}0$⟩, 3) ⟨0001⟩, and 4) ⟨$01\bar{1}1$⟩, respectively (Fig. 6 for reference). In all of these calculations, the single crystal was loaded gradually until the nominal strain reached 15% in the loading direction. The calculated stress−strain relations in the above loading paths are shown in Fig. 7. The behavior of the crystal model is strongly anisotropic.

5.1 Crystal anisotropy and meso analysis

The compression stress−strain curves are plotted with absolute values in order to compare the results with the tension stress−strain curves.

Figure 7 shows the stress−strain curves of AZ31

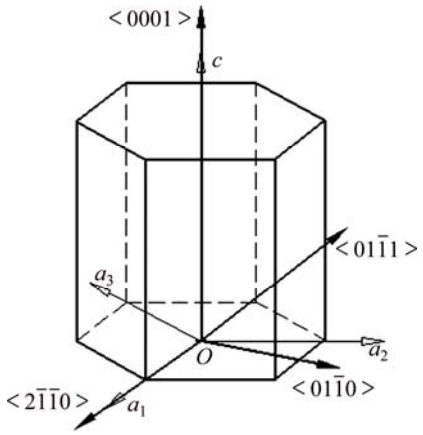

Fig. 6 Loading direction in unit cell

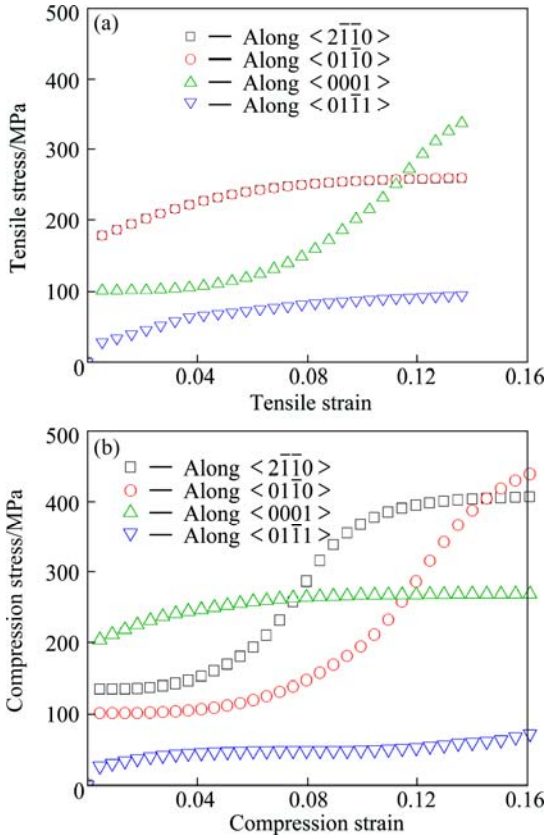

Fig. 7 Stress−strain curves in four different directions

magnesium alloy obtained from simulation investigation under uniaxial tension and compression in four different directions. A careful observation of the stress−strain curves shown in Fig. 7 reveals that the yield stresses are different in four loading paths. During monotonic tension in Fig. 7(a), the yield stresses along $\langle 2\bar{1}\bar{1}0\rangle$ and $\langle 01\bar{1}0\rangle$ occur at the same magnitude of 175 MPa. The plastic deformation is largely caused by the activity of prismatic $\langle a\rangle$ slip and a little compression twin $(1\bar{1}01)\langle 1\bar{1}02\rangle$ (Figs. 8(a) and (c)).

The crystal flows at a near-constant stress of 100 MPa to form a plateau along $\langle 0001\rangle$ loading path due to the activity of tension twin $(1\bar{1}02)\langle\bar{1}101\rangle$ (Fig. 8(e)). As the plastic deformation proceeds until a strain of about 6.5%, tension twinning is exhausted, followed by a flow characterized by a incrementally increased strain hardening rate dominated by prismatic $\langle a+c\rangle$ slip. In addition, when the stress reaches 30 MPa, the material flows in $\langle 01\bar{1}0\rangle$ loading direction due to activity of basal $\langle a\rangle$ slip. And the activity of compression twin $(1\bar{1}01)\langle 1\bar{1}02\rangle$ (Fig. 8(h)) emerges at the strain of approximately 4% and the maximum stress of only about 95 MPa.

During monotonic compression in Fig. 7(b), the stress−strain curves form a plateau at the beginning of material yielding along $\langle 2\bar{1}\bar{1}0\rangle$ and $\langle 01\bar{1}0\rangle$ compression paths. A plateau in $\langle 2\bar{1}\bar{1}0\rangle$ and $\langle 01\bar{1}0\rangle$ compression directions is resulted from the activity of tension twin $(1\bar{1}02)\langle\bar{1}101\rangle$) (Figs. 8(b) and (d)). Furthermore, the material flows at stresses of 140, 100, 200 and 30 MPa in $\langle 2\bar{1}\bar{1}0\rangle$, $\langle 01\bar{1}0\rangle$, $\langle 0001\rangle$ and $\langle 01\bar{1}1\rangle$ strain paths, respectively. The compression yield stress lies on the CRSS of the prismatic $\langle a+c\rangle$ slip system along $\langle 0001\rangle$ direction (Fig. 8(f)). But the compression yield stresses depend on the CRSS of the tension twinning system along $\langle 2\bar{1}\bar{1}0\rangle$ and $\langle 01\bar{1}0\rangle$ directions. The compression yield stresses are different along $\langle 2\bar{1}\bar{1}0\rangle$ and $\langle 01\bar{1}0\rangle$ directions mainly due to different Schmid factors. The plastic deformation along $\langle 01\bar{1}1\rangle$ direction is caused by the activity of basal $\langle a\rangle$ slip (Fig. 8(h)).

The comparative analysis of the stress−strain curves along the above four different directions shows that the flow stresses of tension and compression loading are quite asymmetric. For instance, the flow stress along $\langle 2\bar{1}\bar{1}0\rangle$ tension path is 175 MPa due to the activity of prismatic $\langle a\rangle$ slip. But the flow stress along $\langle 2\bar{1}\bar{1}0\rangle$ compression path is 140 MPa due to the activity of tension twin $(1\bar{1}02)\langle\bar{1}101\rangle$ (Fig. 7).

In conclusion, the yield strength and the macroscopic stress−strain responses are observably dependent upon the combination of slip and twin system activities. And the activity of each slip or twin system is heavily influenced by the CRSS and the loading path. The rate of work hardening and the velocity of stress saturated are affected by the volume fraction of twin. Specifically, the greater the volume fraction of twin is, the higher the rate of work hardening and the saturated stress are.

5.2 Types of twin variants and twin intersection

The theoretical calculations show that not all of twin variants have contribution to the propagation of twin bands in the deformed crystal. It is feasible to theoretically predict which type of twin variant readily

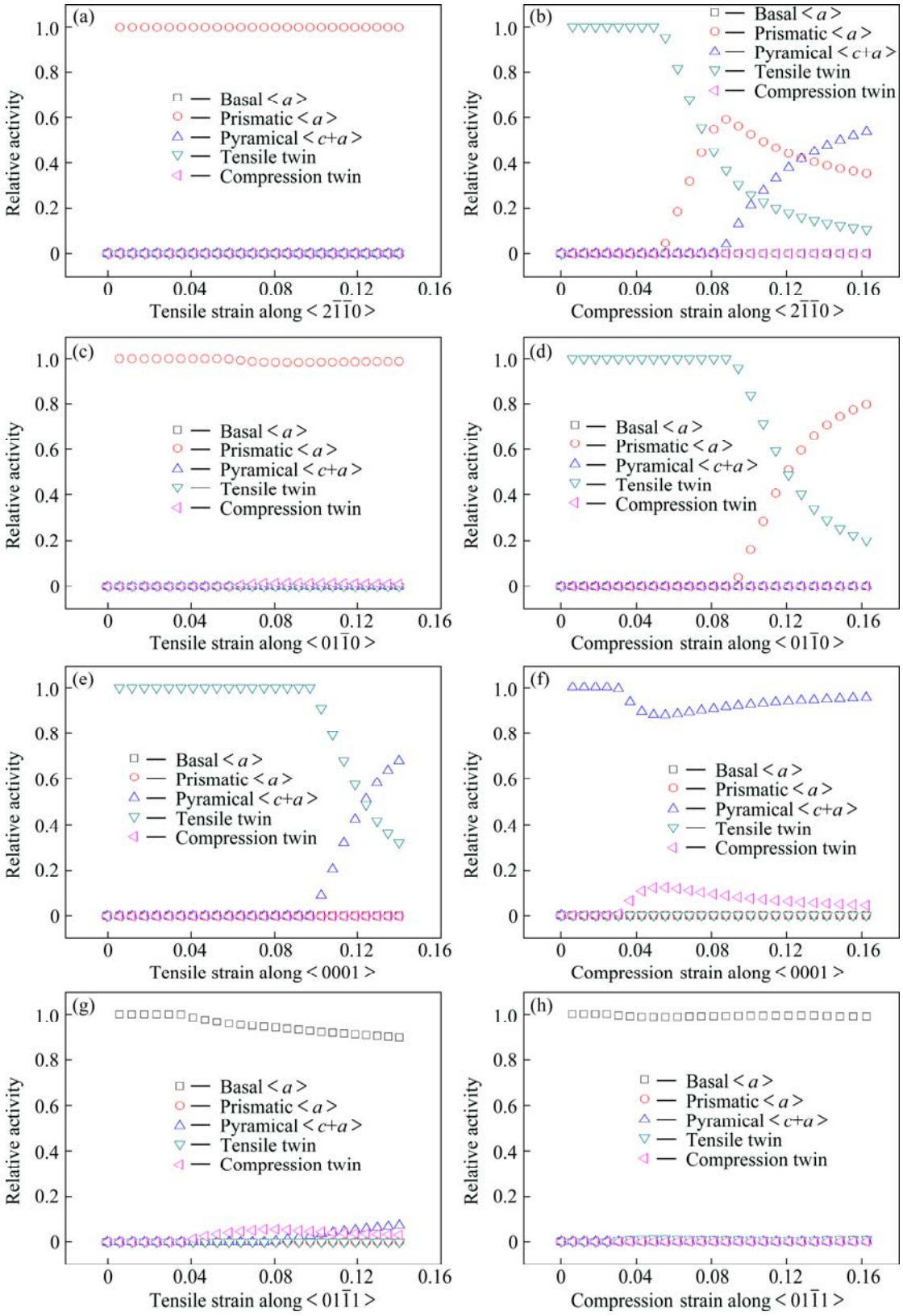

Fig. 8 Relative activities of five deformation modes during uniaxial loading

experiences a reorientation under monotonous loading. The relative activity of twin variants defined in the following equation [18] is used to carry out this.

$$a_{\mathrm{r}}^{\beta,G}=\frac{\int_0^t \dot{\gamma}^{\beta,G}\mathrm{d}t}{\int_0^t\left(\sum_{\alpha}\dot{\gamma}^{\alpha,G}+\sum_{\beta}\dot{\gamma}^{\beta,G}\right)\mathrm{d}t} \tag{38}$$

where $a_r^{\beta,G}$ denotes the relative activity of twin variants; $\dot{\gamma}^{\alpha,G}$ and $\dot{\gamma}^{\beta,G}$ denote the shear rates in slip systems and twin systems, respectively. They are summed up within each GIP at each incremental step during plastic deformation.

Figure 9 shows the relative activities of twin variants calculated for the deformed crystal in different strain paths. Since several types of twin variants emerge in a grain, it is possible to emerge twin intersection and form various types of twin intersection [20]. In Fig. 9, on

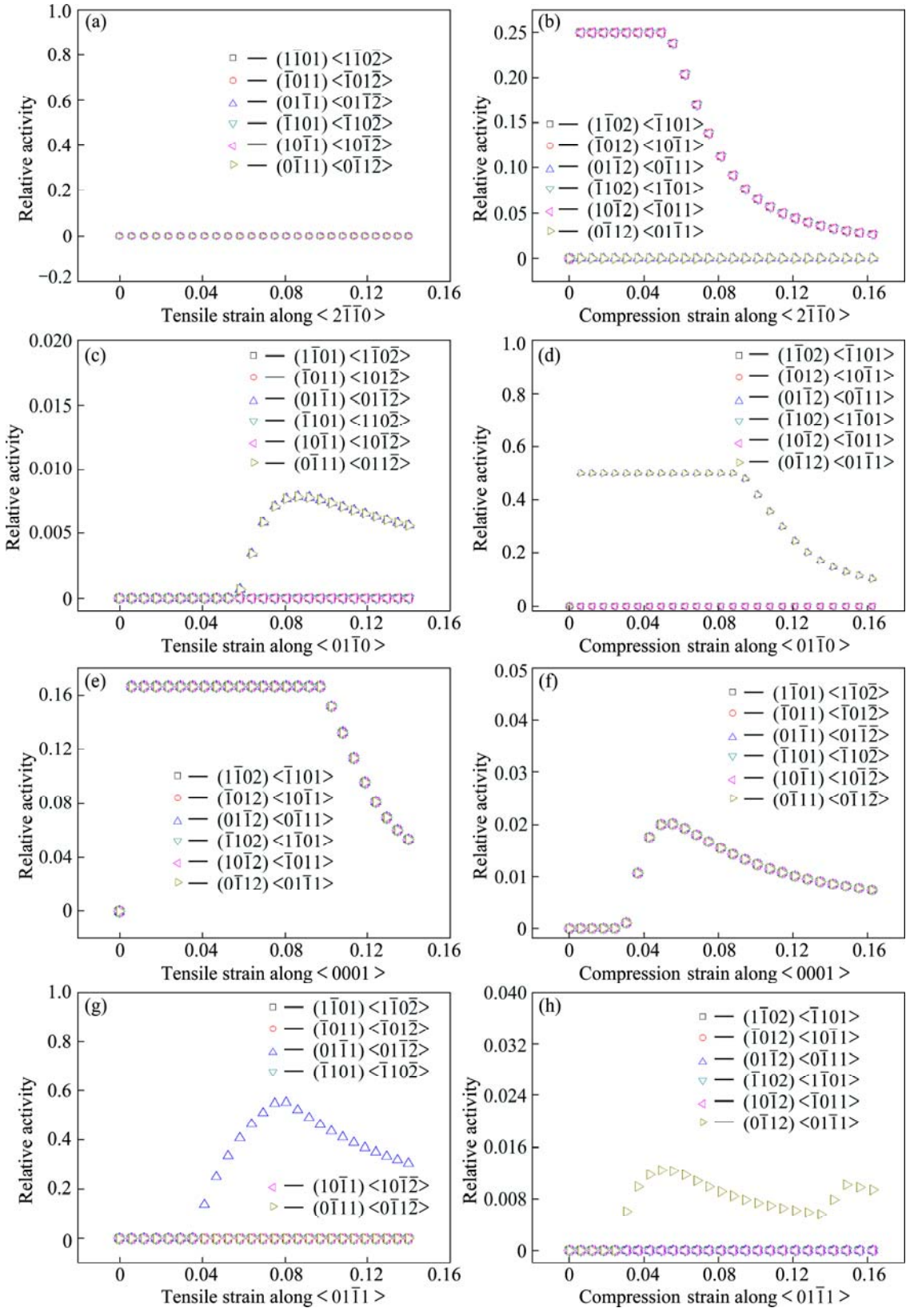

Fig. 9 Relative activities of twin variants during uniaxial loading

one hand, the cases of the activity of tension twin are (a_1) compression along $\langle 2\bar{1}\bar{1}0\rangle$, ($b_1$) compression along $\langle 01\bar{1}0\rangle$, ($c_1$) tension along $\langle 0001\rangle$ and (d_1) compression along $\langle 01\bar{1}1\rangle$. In the case of ($a_1$), there are four types of twin variants to be activated, i.e., $(1\bar{1}02)\ \langle\bar{1}101\rangle$, $(\bar{1}012)\ \langle 10\bar{1}1\rangle$, $(\bar{1}102)\ \langle 1\bar{1}01\rangle$ and $(10\bar{1}2)\ \langle\bar{1}011\rangle$ (Fig. 9(b)). The types of potential twin intersection are $(1\bar{1}02)-(\bar{1}012)$, $(1\bar{1}02)-(\bar{1}102)$ and $(1\bar{1}02)-(10\bar{1}2)$. In the case of ($b_1$), there are two types of twin variants to be activated, i.e. $(01\bar{1}2)\ \langle 0\bar{1}11\rangle$ and $(0\bar{1}12)\ \langle 01\bar{1}1\rangle$ (Fig. 9(d)). The type of potential twin intersection is $(1\bar{1}02)-(\bar{1}012)$. In the case of ($c_1$), there are six types of twin variants to be activated (Fig. 9(e)). The types of potential twin intersection are $(1\bar{1}02)-(\bar{1}012)$, $(1\bar{1}02)-(01\bar{1}2)$, $(1\bar{1}02)-(\bar{1}102)$, $(1\bar{1}02)-(10\bar{1}2)$ and $(1\bar{1}02)-(0\bar{1}12)$. In the case of ($d_1$), there is one type of twin variant to be activated, i.e. $(0\bar{1}12)\ \langle 01\bar{1}1\rangle$ (Fig. 9(h)).

On the other hand, the cases of the activity of compression twin are (a_2) tension along $\langle 2\bar{1}\bar{1}0\rangle$, ($b_2$) tension along $\langle 01\bar{1}0\rangle$, ($c_2$) compression along $\langle 0001\rangle$ and (d_2) tension along $\langle 01\bar{1}1\rangle$. In the case of ($a_2$), there is no type of twin variant to be activated (Fig. 9(a)). In the case of (b_2), there are two types of twin variants to be activated, i.e. $(01\bar{1}1)\ \langle 01\bar{1}\bar{2}\rangle$ and $(0\bar{1}11)\ \langle 0\bar{1}12\rangle$ (Fig. 9(c)). The types of potential twin intersection are $(1\bar{1}01)-(\bar{1}101)$. In the case of ($c_2$), there are all six types of twin variant to be activated (Fig. 9(f)). The types of potential twin intersection are $(1\bar{1}01)-(\bar{1}011)$, $(1\bar{1}01)-(01\bar{1}1)$, $(1\bar{1}01)-(\bar{1}101)$, $(1\bar{1}01)-(10\bar{1}1)$ and $(1\bar{1}01)-(0\bar{1}11)$. In the case of ($d_2$), there is one type of twin variant to be activated, i.e. $(01\bar{1}1)\ \langle 01\bar{1}\bar{2}\rangle$ (Fig. 9(g)).

The above analysis indicates that the number of the active twin variants and the type of the dominant twin variants are also dependent on the orientation of the crystal, which leads to different types of twin intersection. The twin intersection leads to strain hardening due to the mutual interference of intersectional twin. The role of strain hardening is described by the latent hardening parameters in the above constitutive model. Due to the limitation of experimental condition, it is difficult to represent completely the emergence of all types of twin intersection under various loading conditions with experiments. So it is very necessary to analyze all types of twin intersection under various loading conditions by numerical method.

6 Conclusions

1) The constitutive model and hardening functions are utilized to simulate the stress−strain behavior of a AZ31 single crystal undergoing uniaxial loading in four different paths. It is reasonable to predict the plastic behavior of an AZ31 single crystal and the relative activity of slip/twin system in crystal during deformation.

2) The constitutive model and hardening functions can be used to effectively predict the strain hardening characteristics of single crystal. The calculated results reveal that the plastic behavior of an AZ31 single crystal and work hardening are strongly dependent on the loading path, and the single crystal material shows significant anisotropy and asymmetry due to the polar nature of mechanical twinning.

3) Twin variants can be predicted using the model described in Section 3. It is found that the number of active twin variants and the types of dominant twin variants are also heavily dependent on the loading direction, which leads to different types of twin intersection.

4) The rate of work hardening and the velocity of stress saturated are affected by the volume fraction of twin. Namely, the greater the volume fraction of twin is, the higher the rate of work hardening and the saturated stress are.

5) Despite of low CRSS of basal $\langle a\rangle$ system, the relative activity of basal $\langle a\rangle$ slip is not significant during uniaxial loading along $\langle 2\bar{1}\bar{1}0\rangle$ $\langle 01\bar{1}0\rangle$ and $\langle 0001\rangle$ due to the crystal being unfavorably oriented for basal $\langle a\rangle$ slip. On the contrary, relative activity of basal $\langle a\rangle$ slip is dominant in the $\langle 01\bar{1}2\rangle$ monotonic loading path due to favorable orientation of crystal. It is proved that plastic behavior of crystal is heavily dependent on the loading direction.

References

[1] AGNEW S R, MEHROTRA P, LILLO T M, STOICA G M, LIAW P K. Texture evolution of five wrought magnesium alloys during route A equal channel angular extrusion: Experiments and simulations [J]. Acta Mater, 2005, 53: 3135−3146.

[2] WU L, JAIN A, BROWN D W, STOICA G M, AGNEW S R, CLAUSEN B, FIELDEN D E, LIAW P K. Twinning–detwinning behavior during the strain-controlled low-cycle fatigue testing of a wrought magnesium alloy, ZK60A [J]. Acta Materialia, 2008, 56: 688−695.

[3] ZHANG Xue-feng, WU Guo-hua, LIU Wen-cai, DING Wen-jang. Low temperature mechanical properties of as-extruded Mg−10Gd−3Y−0.5Zr magnesium alloy [J]. Transactions of Nonferrous Metals Society of China, 2012, 22(12): 2883−2890.

[4] GANAPATHYSUBRAMANIAN S, ZABARAS N. Design across length scales: A reduced-order model of polycrystal plasticity for the control of microstructure-sensitive material properties [J]. Comput Meth Appl Mech Eng, 2004, 193: 5017−5034.

[5] GANAPATHYSUBRAMANIAN S, ZABARAS N. Modeling the thermoelastic–viscoplastic response of polycrystals using a continuum representation over the orientation space [J]. Int J Plasticity, 2005, 21: 119−144.

[6] TOME C N, LEBENSOHN R A, KOCKS U F. A model for texture development dominated by deformation twinning: Application to zirconium alloys [J]. Acta Metull Muter, 1991, 39: 2667−2680.

[7] JIANG L, JONAS J, MISHRA R, LUO A A, SACHDEV A K, GODET S. Twinning and texture development in two Mg alloys subjected to loading along three different strain paths [J]. Acta Mater, 2007, 55: 3899−3910.
[8] HUANG Shi-yao, ZHANG Shao-rui, LI Da-yong, PENG Ying-hong. Simulation of texture evolution during plastic deformation of FCC, BCC and HCP structured crystals with crystal plasticity based finite element method [J]. Transactions of Nonferrous Metals Society of China, 2011, 21: 1817−1825.
[9] KOUCHMESHKY B, ZABARAS N. Modeling the response of HCP polycrystals deforming by slip and twinning using a finite element representation of the orientation space [J]. Computational Materials Science, 2009, 45: 1043−1051.
[10] ASARO R J, RICE J R. Strain localization in ductile single crystals [J]. J Mech Phys Solids, 1977, 25: 309−338.
[11] KALIDINDI S R. Incorporation of deformation twinning in crystal plasttcity models [J]. J Mech Phys Solids, 1998, 46(2): 267−290.
[12] ZHANG K S, WU M S, FENG R. Simulation of microplasticity-induced deformation in uniaxially strained ceramics by 3-D Voronoi polycrystal modeling [J]. International Journal of Plasticity, 2005, 21: 801−834.
[13] PROUST G, TOMÉ C N, JAIN A, AGNEW S R. Modeling the effect of twinning and detwinning during strain-path changes of magnesium alloy AZ31 [J]. Int J Plasticity, 2009, 25: 861−880.
[14] PAN J, RICE J R. Rate sensitively of plastic flow and implications for yield surface vertices [J]. Int J Solids Struct, 1983, 19: 973−987.
[15] KNEZEVIC M, LEVINSON A, HARRIS R, MISHRA R K, DOHERTY R D, KALIDINDI S R. Deformation twinning in AZ31: Influence on strain hardening and texture evolution [J]. Acta Materialia, 2010, 58: 6230−6242.
[16] LOU X Y, LI M, BOGER R K, AGNEW S R, WAGONER R H. Hardening evolution of AZ31B Mg sheet [J]. International Journal of Plasticity, 2007, 23(1): 44−87.
[17] MARKO K, AMANDA L, RYAN H, DOHERTY R D, KALIDINDI S R. Deformation twinning in AZ31: Influence on strain hardening and texture evolution [J]. Acta Materialia, 2010, 58: 6230−6242.
[18] CHOI S H, SHIN E J, SEONG B S. Simulation of deformation twins and deformation texture in an AZ31 Mg alloy under uniaxial compression [J]. Acta Materialia, 2007, 55: 4181−4192.
[19] KHAN A S, PANDEY A, GNAUPEL-HEROLD T, MISHRA R K. Mechanical response and texture evolution of AZ31 alloy at large strains for different strain rates and temperatures [J]. International Journal of Plasticity, 2011, 27: 688−706.
[20] YANG Xu-yue, ZHANG Lei. Twinning and twin intersection in AZ31 Mg alloy during warm deformation [J]. Acta Metallurgica Sinica, 2009, 45(11): 1303−1308.(in Chinese)

单轴拉伸与压缩加载下 AZ31 镁合金单晶的各向异性塑性行为

蓝永庭[1,2]，钟献词[3]，权高峰[4]，蔺若成[5]，张克实[1]

1. 广西大学 工程防灾与结构安全重点实验室，南宁 530004；
2. 广西科技大学 职业技术教育学院，柳州 545006；
3. 广西大学 数学与信息科学学院，南宁 530004；
4. 西南交通大学 材料科学与工程学院，成都 610031；
5. 大连海事大学 交通运输装备与海洋工程学院，大连 116026

摘 要：为研究 HCP 结构单晶在塑性变形中的变形孪晶和塑性各向异性，采用基于晶体塑性本构理论的有限单元法，建立包含滑移与孪生变形机制的晶体塑性本构关系，发展了以应力作为自变量的牛顿−拉普森迭代方法，通过已有文献的试验数据验证模型的有效性，并利用此模型模拟 AZ31 单晶体在 4 种(即沿 $\langle 2\bar{1}\bar{1}0\rangle$，$\langle 01\bar{1}0\rangle$，$\langle 0001\rangle$和 $\langle 01\bar{1}1\rangle$ 方向)拉伸与压缩变形路径下的塑性变形行为，并获得了相应加载路径下的应力−应变关系曲线。数值计算结果表明，在不同加载路径下该模型可用于预测滑移系或孪生系的活动情况，以及描述孪生变体的活动数量、主要孪生变体和孪生交叉类型。由于机械孪晶具有的极性性质及其在材料非弹性变形中的重要作用，单晶材料表现出显著的各向异性与非对称性。

关键词： AZ31 镁合金；本构模型；单晶体；变形孪生；孪晶变体；孪晶交叉

(Edited by Wei-ping CHEN)